Supplemental Material
Orbital-Selective Two-Dimensional Superconductivity in 2H-NbS_2

Xiangyu Bi[1], Zeya Li[1], Junwei Huang[1], Feng Qin[2,1,*], Caorong Zhang[1], Zian Xu[3], Ling Zhou[1], Ming Tang[1], Caiyu Qiu[1], Peizhe Tang[3,4], Toshiya Ideue[2], Tsutomu Nojima[5], Yoshihiro Iwasa[2], and Hongtao Yuan[1,†]

[1] *College of Engineering and Applied Sciences, National Laboratory of Solid State Microstructures and Jiangsu Key Laboratory of Artificial Functional Materials, Nanjing University, Nanjing 210000, China*

[2] *Quantum Phase Electronic Center and Department of Applied Physics, The University of Tokyo, Tokyo 113-8656, Japan*

[3] *School of Materials Science and Engineering, Beihang University, Beijing 100191, China*

[4] *Max Planck Institute for the Structure and Dynamics of Matter, Center for Free Electron Laser Science, Hamburg 22761, Germany and*

[5] *Institute for Materials Research, Tohoku University, Sendai 980-8577, Japan*

(Dated: October 2021)

CONTENTS

I. Brillouin zone and Fermi surface sheets 2

II. Details for fitting analysis of $H_C(\theta)$ 3

III. $H_{C,\perp}$-T relation and analysis of multiband nature 6

IV. Reproducibility of the $H_{C,\parallel}$-T phase diagram 7

V. Multiband analysis based on different definitions of H_C 8

VI. Experimental results on flakes with gold coating 10

VII. Phase diagram of temperature-dependent critical current 11

VIII. $H_C(\theta)$ under high pressure and its multiband fitting analysis 12

References 13

* Feng Qin: qinfeng@mp.t.u-tokyo.ac.jp

† Hongtao Yuan: htyuan@nju.edu.cn

I. BRILLOUIN ZONE AND FERMI SURFACE SHEETS

This section provides more detailed information of the 2H-NbS_2 crystal, including the crystal structure, electronic structure and the thickness of the samples. Figure S1(a) shows the top view and side view of the hexagonal layered structure of 2H-NbS_2. In each layer, the niobium atoms (blue balls) are sandwiched by sulfur atoms (yellow balls) with the covalent bonds and form the S-Nb-S structure. Each niobium atom forms 6 covalent bonds with the adjacent sulfur atoms, and each sulfur atom forms 3 covalent bonds with the adjacent niobium atoms. The interaction between two adjacent anti-parallel S-Nb-S layers (lower panel, marked by A and B, respectively) is dominated by van der Waals force, making 2H-NbS_2 a typical van der Waals crystal that can be easily exfoliated along the *ab* plane. Such a layered structure provides 2H-NbS_2 with 2D-like energy dispersion [1].

Figure S1(b) shows the Brillouin zone and the Fermi surface of 2H-NbS_2. Two sheets centered at Γ point of the Brillouin zone (marked by $S_{\Gamma 1}$ and $S_{\Gamma 2}$) form the disk-shaped Fermi surfaces, which indicates the isotropic dispersion relation of the energy band; while the third sheet centered at K point (marked by S_K) forms the cylinder-shaped Fermi surface, which indicates that the dispersion relation of this energy band is strongly anisotropic between out-of-plane and in-plane directions. Our first-principles calculation results are in accordance with a comprehensive understanding of the previous calculation report [1].

In order to determine the thickness of the samples we study, we apply atomic force microscope (AFM) characterization for all samples, and provide a typical AFM image in Fig. S1(c). The AFM image indicates that the flake is uniform, whose thickness is about 35 nm. According to the AFM data, our intentionally selected thickness of all the samples in this study has been confirmed within the range of 35 $\sim$ 45 nm. Therefore, compared with the small coherence length merely about 1.07 nm along c direction (obtained from the H_C-T relation in Fig. 1(d)), samples with such thickness are expected to have bulk superconductivity.

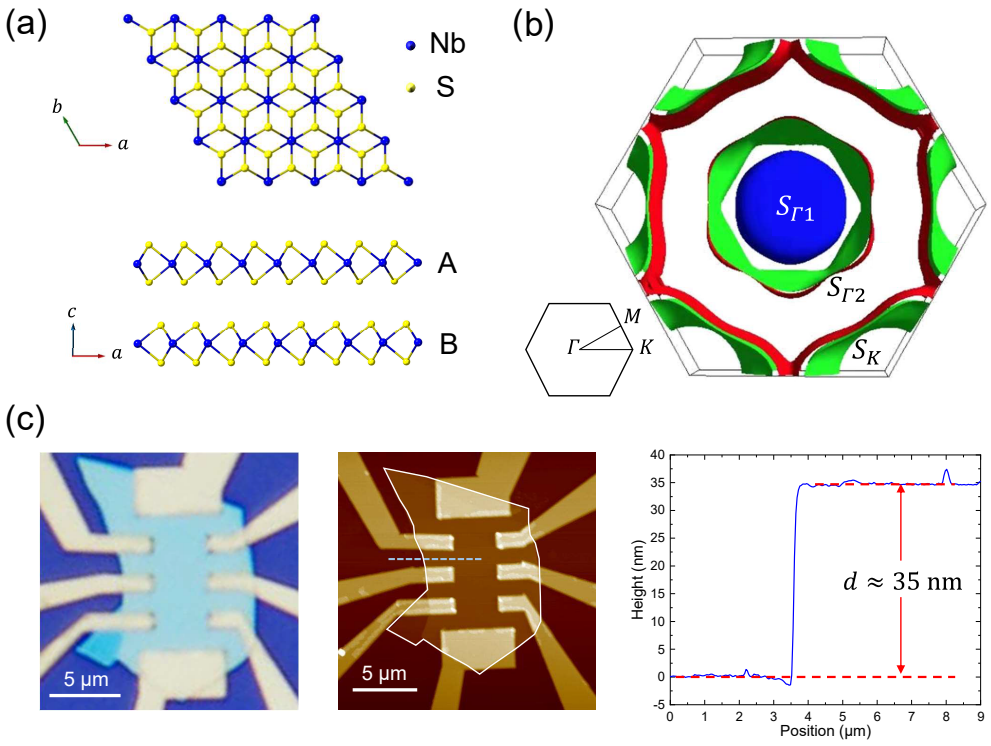

FIG. S 1. Detailed information of 2H-NbS_2 crystal. (a) Schematic crystal structure of 2H-NbS_2 with blue and yellow balls representing Nb and S atoms. The upper panel shows the top view of *ab* plane, and the lower panel shows the side view of bilayer 2H-NbS_2. (b) Brillouin zone and Fermi surface of 2H-NbS_2 based on first-principles calculations. The top view of Brillouin zone together with high-symmetry points is shown at the lower-left corner. (c) Optical photograph, AFM image and the thickness profile of a typical sample with thickness about 35 nm. The scale bars represent 5 μm in optical and AFM images.

II. DETAILS FOR FITTING ANALYSIS OF $H_C(\theta)$

This section shows the detailed fitting process for the discussions presented in the main text (Figs. 2(c)-(e)). As we have mentioned in the main text, the fitting methods of $H_C(\theta)$ is strongly dependent on the temperature, and has to be divided into three analysis ranges. Figure S2 provides the fitting results for the following three cases: (a) single 2D component at T = 5.2 K, (b) "2D and 2D" components at T = 5.0 K, and (c) "2D and 2D and 3D" components at T = 4.5 K. Such fitting results for the whole θ range, together with the partial enlargement of $H_C(\theta)$ curves (θ between 80° and 100°, shown in Figs. 2(c)-(e) in the main text), can provide perfect fitting for our measured data, indicating that our fitting methods are reasonable and appropriate. Since both the H_{C2} and the H_{C3} contribute to the angular distribution of critical magnetic field, here we apply a more general expression $H_C(\theta)$ instead of $H_{C2}(\theta)$ to describe the critical magnetic field. Note that the 2D (green) and 3D (blue) fitting curves seem to be similar when θ is far away from 90°, while they show contrast behavior when θ is near 90°. Thus, the fitting range and fitting formula need to be carefully applied with specific piecewise functions, and we will discuss the detailed fitting processes for different temperature ranges separately in the following three parts.

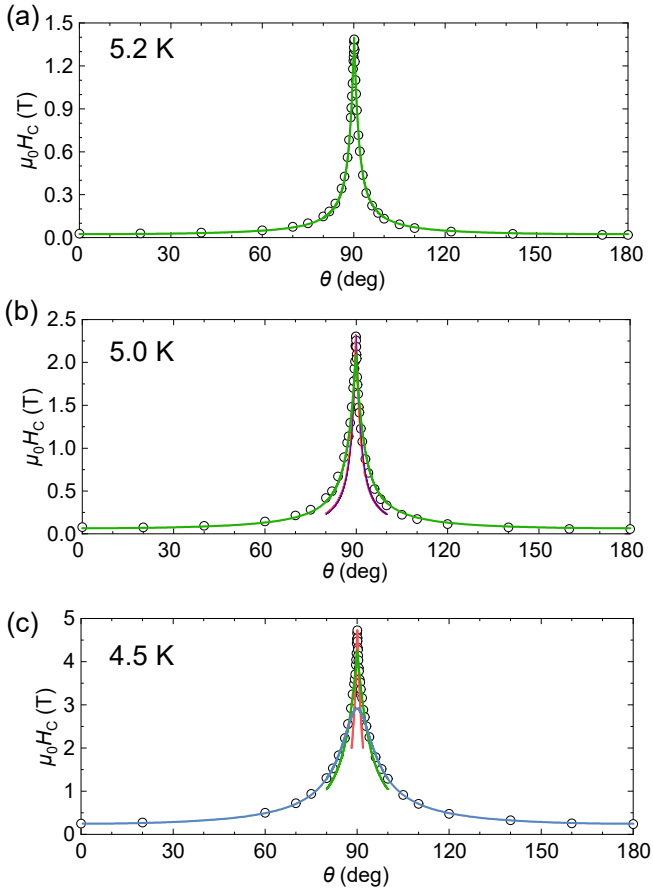

FIG. S 2. The $H_C(\theta)$ fitting with the whole θ range based on the analysis method introduced in the main text, where (a) corresponds to Fig. 2(c) (5.2 K), (b) corresponds to Fig. 2(d) (5.0 K), and (c) corresponds to Fig. 2(e) (4.5 K), respectively. The abovementioned methods can fit the whole θ range well.

In the temperature range of 5.1 K$< T < T_C$, we compare the $H_C(\theta)$ fitting with the single 3D equation (Figs. S3(a) and (b)) based on Eq. (1) to that with the single 2D equation (Fig. S3(c)) based on Eq. (2). As an example, we show the specific comparison at the temperature of 5.2 K. For the fitting with 3D equation, although the fitting in the whole θ range seems to be acceptable (Fig. S3(a)), the enlarged fitting curve at the θ near 90° shows a dome shape and apparently deviates from data points (cusp peak) in Fig. S3(b). Compared with the improper fitting based on the 3D equation, the fitting model with a 2D equation can fit the data better (Fig. S3(c) and Fig. 2(c) in the main text) at this temperature range, particularly for the fitting to the sharp shape of the cusp peak. Since the cusp peak exists in the entire temperature range we study, at least one 2D component needs to

be included in our fitting models.

In the temperature range of 4.8 K$< T \leq$ 5.1 K, one can find from Figs. S3(d) and (e) (5.0 K) that, with only a single 2D equation, the peak is so sharp that we cannot fit the data well near $H \parallel ab$ (partial enlargement for $88^\circ \sim 92^\circ$). Interestingly, once we apply one more 2D equation for fitting based on the piecewise function, this "2D and 2D" model starts to fit the data points better, as shown in Fig. S3(f). Note that these two "2D" peaks are very close to each other in this temperature range, while one can see a clear separation of these two peaks at a lower temperature, for example, from the fitting results at 4.5 K (inset of Fig. 2(e)). Therefore, it is reasonable to apply two 2D superconducting components in our fitting model for the data in those temperatures from 4.8 K to 5.1 K.

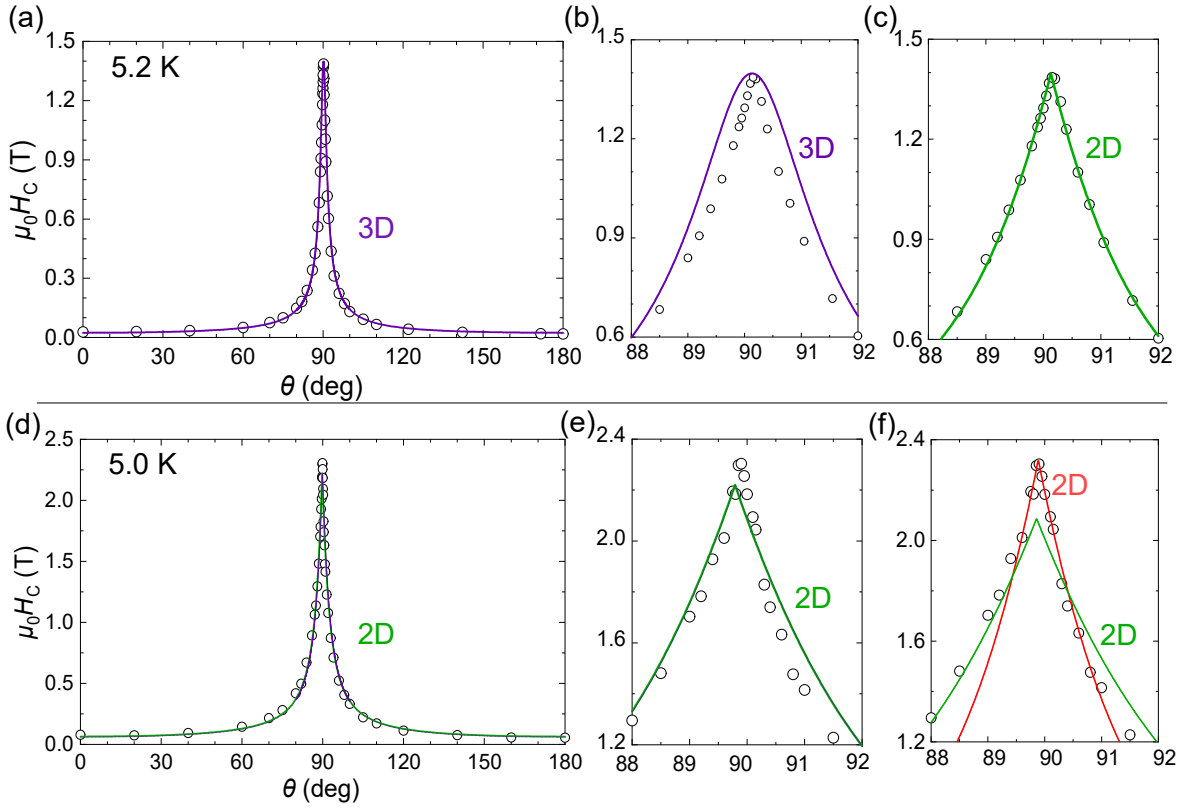

FIG. S 3. The comparison of different fitting methods. (a-c) Comparison between single 3D Ginzburg-Landau fitting curve and single 2D Tinkham fitting curve at T = 5.2 K, with the $H_C(\theta)$ fitting for (a) the whole θ range and (b) its partial enlargement from 88° to 92°. Compared with the better fitting obtained from the 2D Tinkham equation shown in (c), the 3D fitting curve from Ginzburg-Landau equation fails to fit the data points at 5.2 K in this enlarged range. (d-f) Comparison between single 2D Tinkham fitting result and "2D and 2D" Tinkham fitting results at T = 5.0 K. (d) is the single 2D fitting for the whole θ range, (e) is its partial enlargement between 88° and 92°, and (f) is the "2D and 2D" fitting result in this enlarged range. Obviously, the fitting model based on two 2D components helps us achieve better fitting than that based on the fitting model with a single 2D component.

Finally, in the temperature range of 2.6 K$< T \leq$ 4.8 K, we take the $H_C(\theta)$ data at 2.8 K as an example for our fitting analysis (Fig. S4(a)), and one can see two turning points at $90 \pm 0.4^\circ$, which indicates that at least two superconducting components are required for a better fitting with a piecewise function divided by the two turning points. However, although we have tried the abovementioned analysis method based on the "2D and 2D" fitting model with the piecewise function, we cannot well fit the $H_C(\theta)$ data no matter how we adjust the parameters of the piecewise function. On the other hand, considering the existence of the 3D superconducting sub-band in 2H-NbS_2 thick flake, it is reasonable to introduce an anisotropic 3D superconducting component in our fitting model. Therefore, we finally adopt a "2D and 2D and 3D" model to fit the $H_C(\theta)$ data at this temperature range. As expected, the "2D and 2D and 3D" model can fit the $H_C(\theta)$ data better than the "2D and 2D" model. More details for the corresponding comparison are given as follows:

Although we apply "2D and 2D" (Fig. S4(b)) and "2D and 3D" (Fig. S4(c)) models to fit the $H_C(\theta)$ relation, neither of these two fitting methods can fit the experimental results accurately: For the "2D and 3D" model, the $H_C(\theta)$ cannot be fitted

well for the whole θ range (Fig. S4(c)); while for the "2D and 2D" model, the fitting curve still deviates apparently from the data points in the ranges $0^\circ \leq \theta < 89.6^\circ$ and $90.4^\circ < \theta \leq 180^\circ$, even though the $H_C(\theta)$ can be well fitted in the region inside the two turning points (inset figure of Fig. S4(b)). No matter how we adjust the fitting ranges and parameters in our piecewise function, the fitting curves cannot fit the experimental data well. More importantly, since we have deduced in the main text (Fig. 1(d)) that the sample is a bulk superconductor and we have observed the 3D-like behavior in the low temperature range, it is self-consistent only when the 3D component is introduced in this system at low temperatures. Therefore, one more 3D superconducting component has to be added.

Figure S4(d) shows the fitting results with the "2D and 2D and 3D" model for the data at 2.8 K, and the inset shows its partial enlargement for $88^\circ \sim 92^\circ$. In the piecewise function, there are the following three components: a sharp 2D component fits the data in the range $90 \pm 0.2^\circ$, the other 2D component fits the data in the range $88^\circ \sim 89.8^\circ$ and $90.2^\circ \sim 92^\circ$, and a 3D component fits all the other ranges. This three-component model can fit the experimental results well, as shown in Fig. S4(d). Since such a three-component model (2D and 2D and 3D) can fit all the other $H_C(\theta)$ relations for temperature $T \leq 4.8$ K, no more fitting curves are necessary.

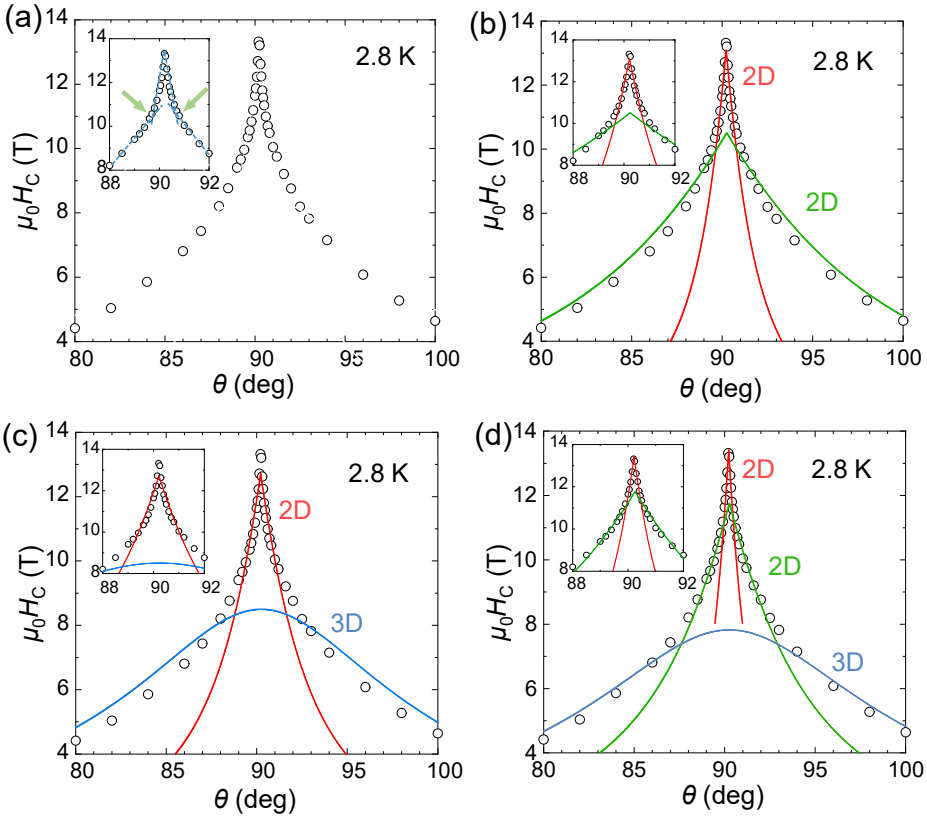

FIG. S 4. Fitting methods comparison of the $H_C(\theta)$ at 2.8 K. (a) The $H_C(\theta)$ data points and the partial enlargement in the range of $88^\circ \sim 92^\circ$. The sharp peak at 90° clearly implies the existence of a 2D superconducting component. The two light green arrows at 89.6° and 90.4° (intersections of the blue dashed lines) denote the turning points in $H_C(\theta)$ data. (b,c) Fitting results based on "2D and 2D" (b), and "2D and 3D" (c) models. Neither of these two models can fit the data well. (d) Fitting results based on "2D and 2D and 3D" model, where the red and green fitting curves are both associated with the 2D Tinkham equation, and the blue fitting curve is associated with the 3D Ginzburg-Landau equation. This three-component model can fit the $H_C(\theta)$ data points well.

III. $H_{C,\perp}$-T RELATION AND ANALYSIS OF MULTIBAND NATURE

As a further support to the multiband analysis based on $H_{C,\parallel}$, we provide the fitting results of $H_{C,\perp}$-T relation by the above-mentioned "2D and 2D and 3D" model, and analyze the multiband nature of superconducting 2H-NbS_2. Note that the fitting results of $H_{C3,\perp}(2D)$ based on the 2D Tinkham equation remains extremely small and covered by the other two components in the whole temperature range. This can be directly caused by the existence of surface superconductivity [2, 3]. Therefore, as shown in Fig. S5, the $H_{C,\perp}$ originates from two intrinsic components, *i.e.*, the intrinsic 2D and 3D components, as mentioned in the main text. For $T > 4.8$ K, the value of $H_{C2,\perp}(3D)$ (blue balls) is smaller than that of $H_{C2,\perp}(2D)$ (green balls), which serves as the reason why a single 2D component based on the 2D Tinkham equation is good enough for fitting the data at 5.3 K and 5.2 K (Fig. 2(c)). As the temperature decreases, the $H_{C2,\perp}(3D)$ values keep increasing and then becomes larger than the values of $H_{C2,\perp}(2D)$ at about 4.8 K, so the observed $H_{C2,\perp}$ should take the values of the $H_{C2,\perp}(3D)$.

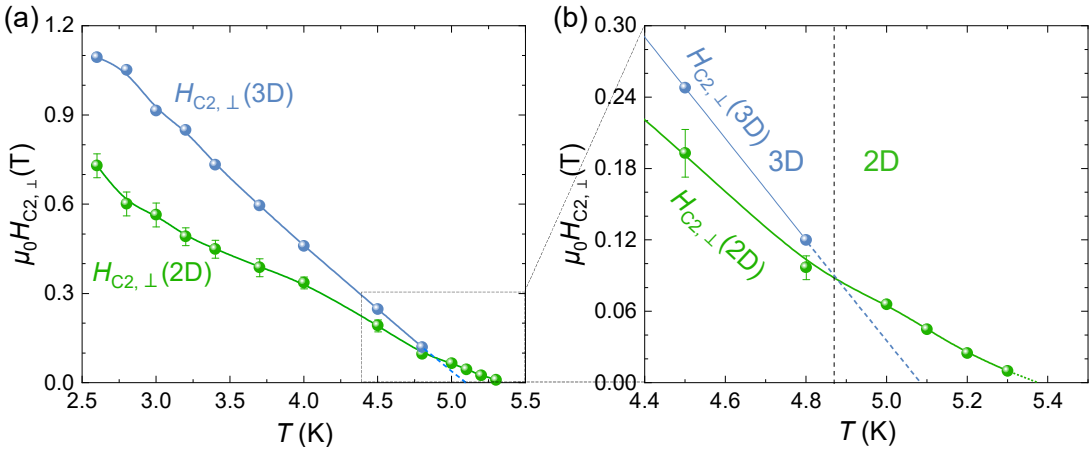

FIG. S 5. The $H_{C,\perp}$-T relation based on $H_C(\theta)$ fitting with "2D and 2D and 3D" model. (a) Temperature dependence of $H_{C2,\perp}$ values according to fitting results. The 2D and 3D components of $H_{C2,\perp}$ are marked by green and blue balls and linked by B-spline curves. (b) Partial enlargement of the $H_{C,\perp}$-T relation from 4.4 K to 5.5 K. The $H_{C2,\perp}(3D)$ component is extrapolated linearly to zero field, marked by the blue dashed line. The black vertical dashed line represents the specific temperature for the crossover of two components. Note that, depending on the temperature range, both the intrinsic 2D and 3D components contribute to the observed $H_{C2,\perp}$.

The above results can provide information about the multiband nature of superconducting 2H-NbS_2, where one sub-band shows 2D-like behavior, and the other shows 3D-like behavior. This is consistent well with previous calculation results[1] and can well explain our observation of the concaved shape of the out-of-plane critical field $H_{C,\perp}$ (Fig. 1(d)).

IV. REPRODUCIBILITY OF THE $H_{C,\parallel}$-T PHASE DIAGRAM

In order to verify the reproducibility of the $H_{C,\parallel}$-T relation discussed in the main text (Figs. 3(a) and (c), Fig. 4(b)), we fabricate another type of devices with 2H-NbS_2 surface partially covered by Au film (7 nm thick), and notice that the Au-capped 2H-NbS_2 also displays the similar $H_{C,\parallel}$-T relation to those devices without Au capping. Figure S6(a) is an optical image of the device, and the four-terminal resistances from two measurement channels are presented below. The $H_{C,\parallel}$-T phase diagrams derived from channel 1 (covered by 7 nm-thick Au, electrodes 7-8-9-6) and channel 2 (without Au coverage, electrodes 7-10-12-6) are shown in Figs. S6(b) and (c). Note that there are still three superconducting components in this case, similar to what we have discussed in the main text (Figs. 3(a) and (c), and 4(b)). We can still observe the crossover between the $H_{C2,\parallel}(2D)$ and the $H_{C3,\parallel}(2D)$ near 5.2 K, even though the data points are relatively sparse. Therefore, the coexistence of the 2D and 3D superconductivity components in 2H-NbS_2 is a reproducible feature in our measurement. In addition, the difference between channels with and without Au coverage and the resulted suppression of H_{C3} will be further discussed in detail in Section VI.

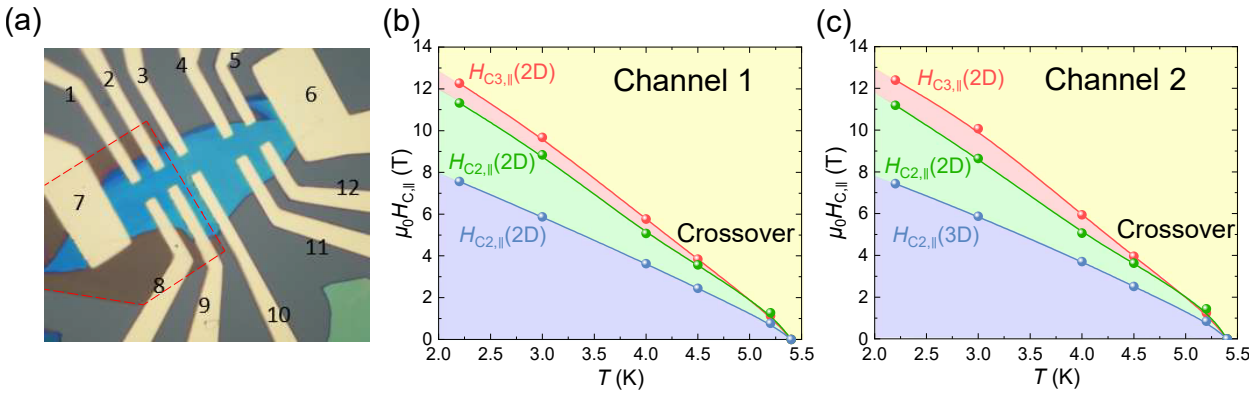

FIG. S 6. The reproducible $H_{C,\parallel}$-T phase diagram of 2H-NbS_2. (a) Optical image of the device. The region covered by 7 nm-thick Au is labelled by the red dashed line. The $H_{C,\parallel}$-T relation derived from two measurement channels are shown in (b) and (c), where channel 1 (electrodes 7-8-9-6) is capped by 7 nm-thick Au, and channel 2 (electrodes 7-10-12-6) has no Au coverage. Surface superconductivity $H_{C3,\parallel}(2D)$, intrinsic 2D superconductivity $H_{C2,\parallel}(2D)$ and intrinsic 3D superconductivity $H_{C2,\parallel}(3D)$ components are marked by balls and curves in red, green and blue. The fitting results are almost the same as we present in Figs. 3(a) and (c).

V. MULTIBAND ANALYSIS BASED ON DIFFERENT DEFINITIONS OF H_C

In order to make a more systematical $H_C(\theta)$ analysis of superconducting 2H-NbS_2, we define H_C by a variety of percentages of R_N (defined as "%R_N", where R_N is the R_{xx} value at T = 6.5 K) for the whole temperature range, and accordingly we fit the $H_C(\theta)$ data (introduced in Section II). Figure S7 displays the extracted $H_{C,\|}$ values, including the values of the $H_{C3,\|}(2D)$ in Fig. S7(a), the $H_{C2,\|}(2D)$ in Fig. S7(b), and the $H_{C2,\|}(3D)$ in Fig. S7(c). For all the experimental data, we can see that the $H_{C,\|}$ values increase as the percentage of %R_N increases, which is in agreement with the R_{xx}-$\mu_0 H$ relations. Since the applied fitting model at the temperature above 4.8 K (discussed in the main text) does not require all three components, certain curves at several temperatures cannot be provided in Figs. S7(a) and (c).

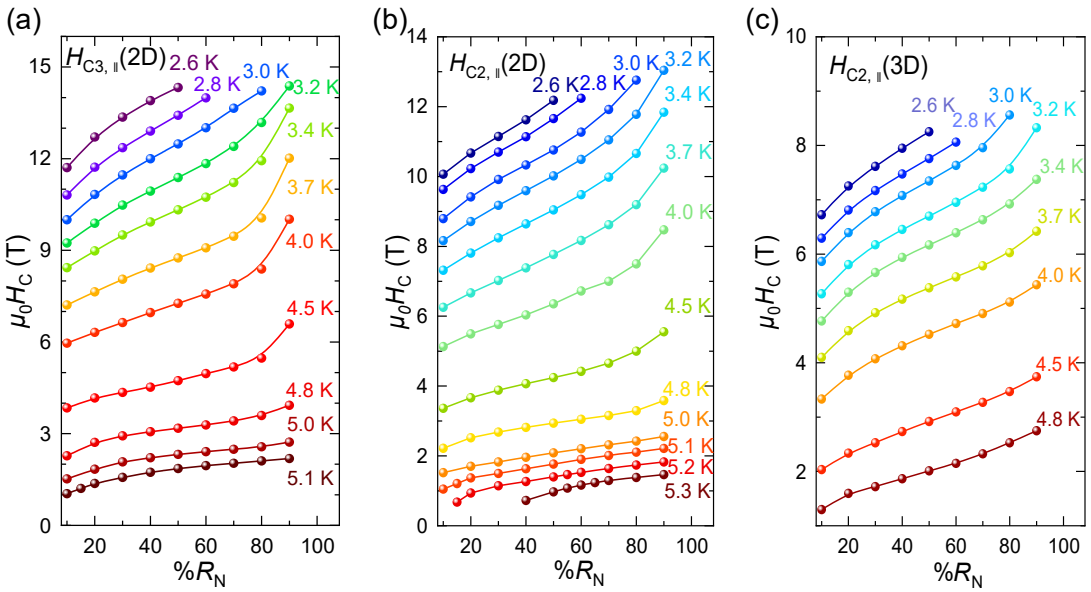

FIG. S 7. Fitting results for H_C defined by different percentages of R_N from 10% to 90%. The horizontal axis shows the percentage of R_N used for defining H_C, and the vertical axis shows the $H_{C,\|}$ values extracted from fitting. The fitting results for three superconducting components at different temperatures are presented as (a) $H_{C3,\|}(2D)$, (b) $H_{C2,\|}(2D)$ and (c) $H_{C2,\|}(3D)$.

Correspondingly, we plot a temperature-dependent phase diagram about the superconductivity behavior of 2H-NbS_2 with different H_C definitions, as shown in Fig. S8. The superconducting regions filled with green, red and blue colors correspond to the fitting analysis with "Single 2D", "2D and 2D", and "2D and 2D and 3D" components, as discussed in Section II. Outside the superconducting region, the normal metal phase is presented in yellow area. Therefore, the dashed line between the green and yellow regions indicates the superconducting phase transition, whose T_C values depend on the percentages of R_N applied for the definition. Similarly, we observe the crossover between superconducting phases with "Single 2D" and "2D and 2D" components, as indicated by the dashed line between the red and green regions. The exact value of crossover temperature depends on the percentages of R_N applied for definition. The superconductivity behavior beyond $\mu_0 H_{C3,\|} = 14$ T is not analyzed here due to the limited magnetic field of our low-temperature magnet facility (the white region at the bottom-right corner). As a reasonable deduction, the "2D and 2D and 3D" model can still fit the superconductivity behavior within this region.

Finally, in order to provide detailed information about the homogeneity of superconductivity, we focus on the starting and ending points of superconducting transition. In particular, we provide the $H_{C,\|}$-T relations with the H_C defined by 20%R_N near zero resistance (Fig. S9 (a)) and by 80%R_N near the onset of superconducting transition (Fig. S9 (b)). Together with the $H_{C,\|}$-T relations with 50%R_N definition discussed in Figs. 3(a) and (c), all the three definitions for H_C mentioned-above can lead to similar $H_{C,\|}$-T relations, indicating the homogeneity of superconductivity in our 2H-NbS_2 sample.

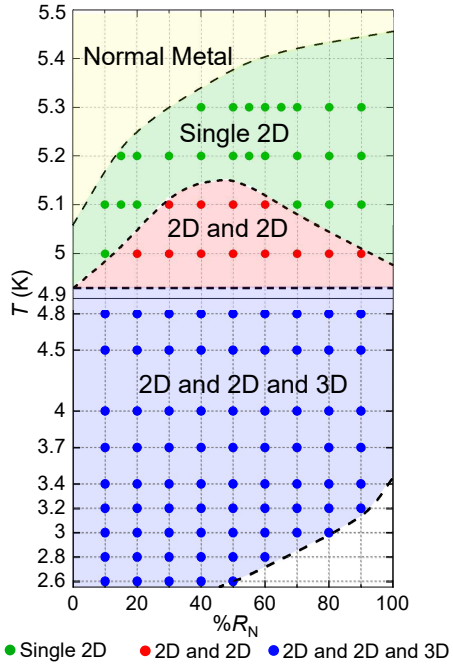

FIG. S 8. Phase diagram and fitting model of 2H-NbS_2 depending on the R_N-percentage ($\%R_N$). The green, red and blue solid circles and filled regions correspond to the applied fitting models with "Single 2D", "2D and 2D", and "2D and 2D and 3D" superconducting components. The yellow region represents the normal metal state. The dashed lines are a guide for eyes and can indicate the boundaries between regions with different fitting models.

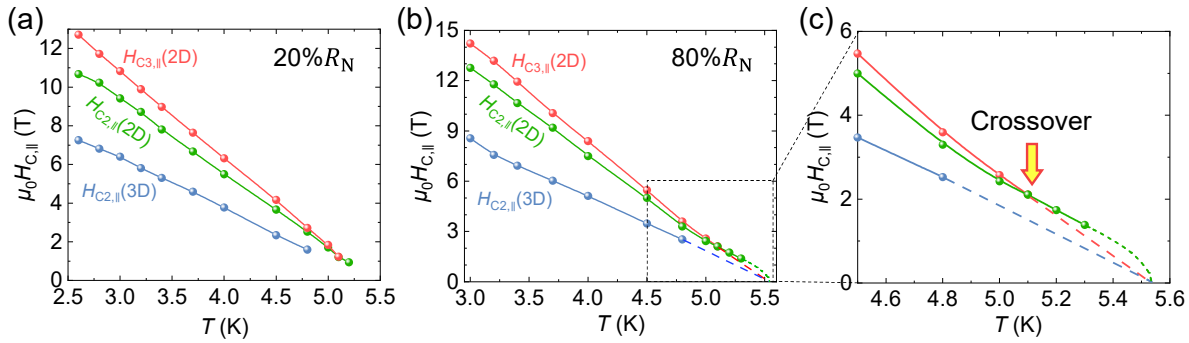

FIG. S 9. Comparison of the $H_{C,\parallel}$-T relations where the H_C are defined by $20\%R_N$ (a) and $80\%R_N$ (b,c). The surface superconducting component $H_{C3,\parallel}(2D)$, intrinsic 2D superconducting component $H_{C2,\parallel}(2D)$ and intrinsic 3D superconducting component $H_{C2,\parallel}(3D)$ are marked by red, green and blue balls, respectively. (c) The partial enlargement of $H_{C,\parallel}$-T relation of (b) near T_C, where one can see a crossover (marked by the yellow arrow) between the red and green curves, indicating the crossover between the intrinsic 2D superconducting component $H_{C2}(2D)$ and the surface superconducting component $H_{C3}(2D)$. This is consistent with what we have discussed in Fig. 3(c) in the main text.

VI. EXPERIMENTAL RESULTS ON FLAKES WITH GOLD COATING

It is commonly agreed that, based on the anti-proximity effect, one can eliminate surface superconductivity via contacting a non-superconducting metal (for instance, Au) to the superconductor [2, 3]. In order to prove that the 2D component we observe (green balls in Fig. 3) is an intrinsic behavior rather than the surface superconductivity of the NbS_2/SiO_2 interface, we sandwich the sample by two Au layers at both surfaces of 2H-NbS_2, and perform the $H_C(\theta)$ measurement. To realize such a structure, we first evaporate 3 nm Ti and 12 nm Au on a small region of SiO_2/Si substrate, and then transfer the exfoliated sample on Au pad in N_2 glove box. Finally, we evaporate 10 nm Au on a part of the sample surface, as shown in Fig. S10(a). The exfoliation and transfer procedures are both conducted with the protection of N_2, so the bottom surface of 2H-NbS_2 is a clean superconductor-metal interface, which is the main focus of this section.

As shown in Figs. S10(b) and (c), the fitting model with "2D and 2D and 3D" superconducting components is still valid, which does not depend on the surface gold coverage. Two things should be addressed here: On one hand, the maximum of the $H_{C2}(3D)$ with and without Au coverage are almost the same, and it is the same situation for the $H_{C2}(2D)$ values. These phenomena can support our expectation that these two superconducting components are related to the intrinsic superconducting behavior of 2H-NbS_2, irrespective of the surface deposition of Au film. On the other hand, one can see that the maximum of $\mu_0 H_{C3}(2D)$ with surface Au coverage decreases more than 1 T compared to that of the channel without surface Au coverage (guided by the red horizontal dashed line). Such suppression of the $H_{C3}(2D)$ can be well explained by the anti-proximity effect. One can conclude that the 2D superconducting component $H_{C2}(2D)$, different from the sharp-2D component $H_{C3}(2D)$ that associated with surface superconductivity, does not originate from the bottom superconductor-metal interface (NbS_2/Au interface) since this surface should be clean enough.

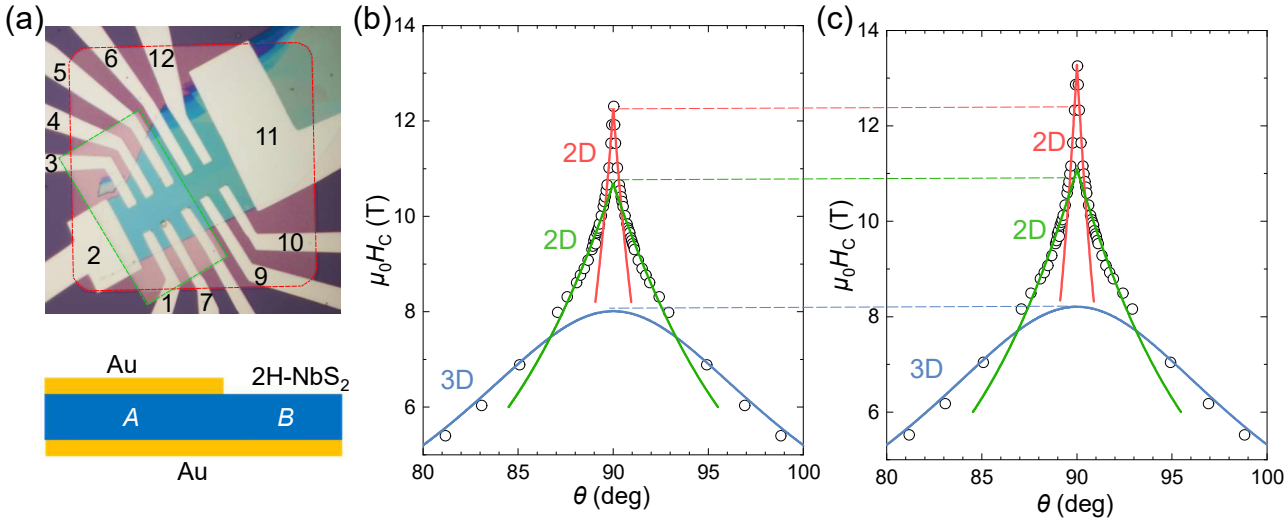

FIG. S 10. The $H_C(\theta)$ relation based on Au/NbS_2/Au sandwich structure. (a) Optical image and schematic side view of the Au/NbS_2/Au device, where the green dashed rectangle represents the area capping with Au film (10 nm) on-top, and the red dashed square represents the Au film (3 nm Ti and 12 nm Au) area below the sample. The yellow and blue rectangles of the side view represent Au film and 2H-NbS_2 flake, and the areas marked by "*A*" and "*B*" correspond to the regions with dual-Au-capping (*A*) and with Au film only at bottom (*B*). (b,c) Comparison of the $H_C(\theta)$ at 3 K with dual-Au-capping (b, electrodes 2-7-8-11, corresponding to area *A*) and with Au film only at bottom (c, electrodes 2-6-12-11, corresponding to area *B*). The three fitting components $H_{C3}(2D)$, $H_{C2}(2D)$, $H_{C2}(3D)$ are marked by red, green and blue. The $H_{C2,\|}$ values of two intrinsic superconducting components (green and blue curves) remain similar in (b) and (c), as presented by the dashed lines in green and blue. The $H_{C3,\|}(2D)$ value associated with surface superconducting component significantly decreases with dual-Au-capping (the maximum of $\mu_0 H_{C3,\|}(2D)$ is about 12.26 T in (b) and 13.30 T in (c)). The data points among $90^\circ \sim 180^\circ$ are obtained by symmetrizing the $0^\circ \sim 90^\circ$ data after reaching the maximum critical magnetic field.

VII. PHASE DIAGRAM OF TEMPERATURE-DEPENDENT CRITICAL CURRENT

To check the influence of the electrical current on the T_C and the deviation from the equilibrium state, we perform temperature-dependent critical current measurement to achieve the I_C-T phase diagram. Figure S11 shows the I_C-T relations and the fitting results based on the empirical formula $I_C(T) = I_C(0\ \mathrm{K})\sqrt{1-(T/T_C)^2}$. The critical current I_C at zero temperature are both in the order of 1000 μA, and the current of about 250 μA will only cause the decrease of T_C for about 5% ($\sim$ 0.3 K) for both samples. Therefore, we expect that the current we apply (250 μA) will not influence the T_C much, and that the system deviates from the equilibrium state very little, so the intrinsic superconducting properties can still be maintained in the samples with the similar thickness (Figs. 4(a)-(c)). Thus, the intrinsic superconducting properties remain the same as those in previous measurements with small electric current (Figs. 2(c)-(e), Figs. 3(a) and (c)).

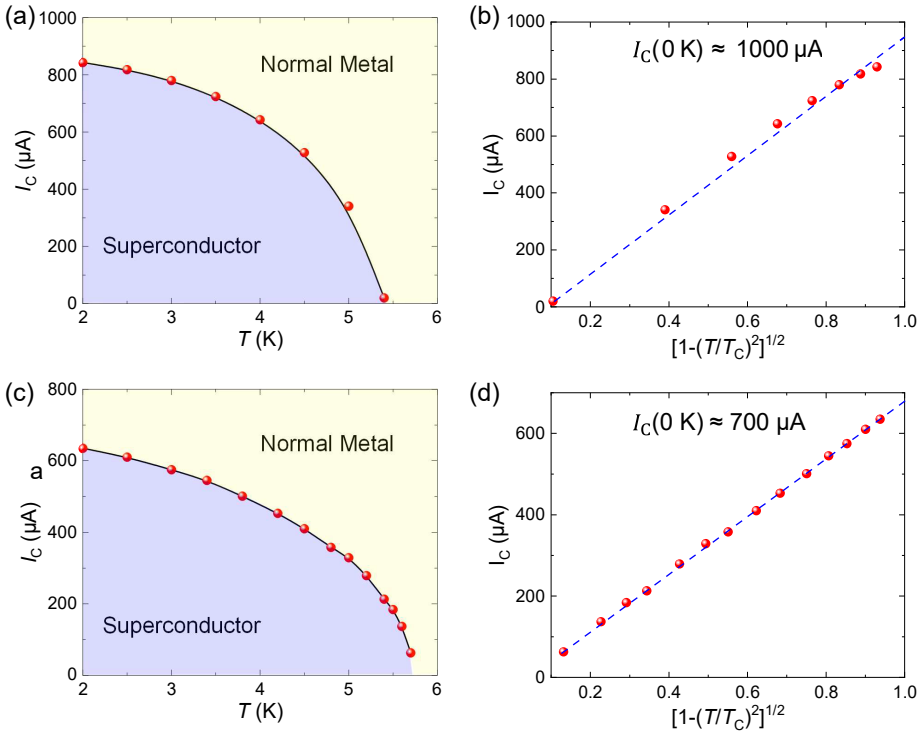

FIG. S 11. Experimental and fitting results of the I_C-T phase diagram of two different samples with similar thickness to that of the particular sample we study in the main text. (a,b) The I_C-T relation and the fitting results based on $I_C(T) = I_C(0\ \mathrm{K})\sqrt{1-(T/T_C)^2}$. (c,d) The I_C-T relation and the same I_C fitting for another sample. The data points in (b) and (d) are connected by B-splines (solid lines). The critical electrical currents at zero temperature for these two samples are estimated to be 1000 μA (b) and 700 μA (d).

VIII. $H_C(\theta)$ UNDER HIGH PRESSURE AND ITS MULTIBAND FITTING ANALYSIS

In this part, to further prove that surface superconductivity can be effectively suppressed by high pressure (as previously reported [4]), while the intrinsic 2D component can still be maintained, we conduct $H_C(\theta)$ measurement under high pressure. One can see that the resulted $H_C(\theta)$ fitting is consistent with Fig. 4(e) in the main text. Figure S12(a) provides the $H_C(\theta)$ relation under 3.2 GPa at 2.2 K (the same temperature as Fig. 4(e)), and Fig. S12(b) is the partial enlargement within the θ range from 80° to 100°. Based on the piecewise function for $H_C(\theta)$ fitting, the "2D and 3D" model is applied, where the 2D component fits the range of 80° $\sim$ 100° and the 3D component fits the other θ ranges (0° $\sim$ 80° and 100° $\sim$ 180°). The fitting ranges for the piecewise function are almost the same as those under the pressure of 4.1 GPa (Fig. 4(e) in the main text). One can also see that only one 2D component exists under 3.2 GPa, which is consistent with the observation under 4.1 GPa. More importantly, the $\mu_0 H_{C2,\parallel}(2D)$ value of 10.11 T at 3.2 GPa is larger than that of 9.33 T at 4.1 GPa, implying that higher pressure can suppress the superconducting anisotropy by reducing the van der Waals gap and enhancing the interlayer coupling.

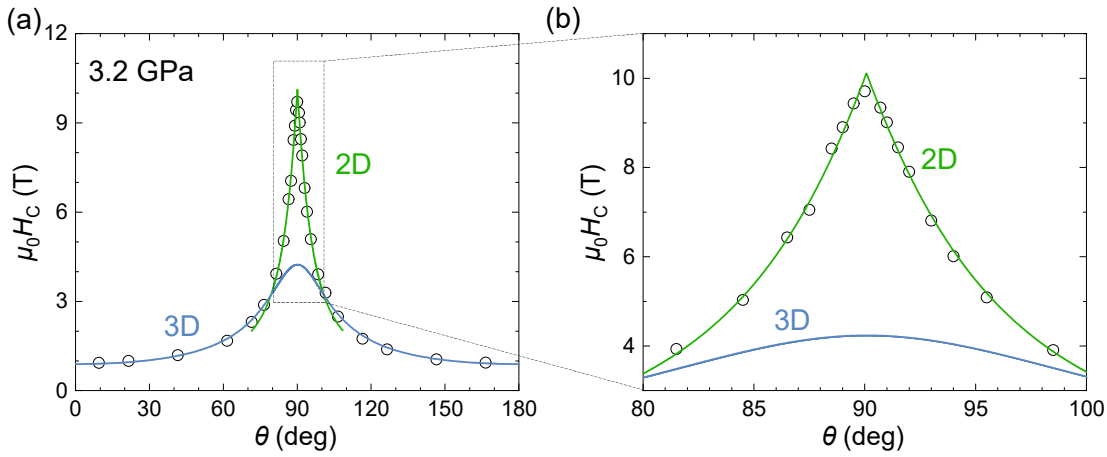

FIG. S 12. Fitting results for $H_C(\theta)$ relation under 3.2 GPa at 2.2 K. (a) The $H_C(\theta)$ relation and fitting curves of "2D and 3D" components in the θ range from 0° to 180°. (b) Partial enlargement of (a) for the θ from 80° to 100°. One can see that a single 2D superconducting component (green curve) can fit the experimental results well near $\theta = 90°$.

[1] C. Heil, S. Poncé, H. Lambert, M. Schlipf, E. R. Margine, and F. Giustino, Origin of superconductivity and latent charge density wave in NbS_2, Phys. Rev. Lett. **119**, 087003 (2017).
[2] M. Tinkham, *Introduction to Superconductivity* (Courier Corporation, 2004).
[3] V. V. Schmidt, *The Physics of Superconductors: Introduction to Fundamentals and Applications*, edited by P. Muller and A. V. Ustinov (Springer Science & Business Media, 1997).
[4] S. Gabáni *et al.*, High-pressure effect on the superconductivity of YB_6, Phys. Rev. B **90**, 045136 (2014).